Efficient solar-driven electrocatalytic nitrate-to-ammonia conversion by 2D ultrathin Fe single-atom catalysts

Ji Li, Weiqi Zhong, Kai Wu, Eddy Petit, Luc Lajaunie, Kun Qi, Yang Zhang, Huali Wu, Jiefeng Liu, Jing Heng, et al.

Efficient solar-driven electrocatalytic nitrate-to-ammonia conversion by 2D ultrathin Fe single- atom catalysts†

Ji Li, *[ab] Weiqi Zhong,[a] Kai Wu,[a] Eddy Petit,[b] Luc Lajaunie, [cd] Kun Qi, [e] Yang Zhang,[b] Huali Wu,[f] Jiefeng Liu,[b] Jing Heng,[a] Xuechuan Wang, [a] Qingxin Han, [a] Taotao Qiang [a] and Damien Voiry *[b]

The controllable design of single-atom electrocatalysts with high active site exposure density, enhanced mass/volume specific activity, and low mass transfer resistance holds tremendous potential for green ammonia synthesis involving the electrochemical nitrate reduction reaction (eNO_3RR). Here we report the synthesis of ultrathin two-dimensional electrocatalysts with the inclusion of iron (Fe) single-atom catalytic active sites (2D Fe-SACs) for the nitrate reduction reaction (NO_3RR). Our isotopic nuclear magnetic resonance (NMR) analyses revealed that 2D Fe-SACs exhibit remarkable performance, with a maximum faradaic efficiency of 95.4 ± 4.00% for the NO_3RR to NH_3 at an overpotential of −0.40 V *versus* the reversible hydrogen electrode (*vs.* RHE). Density functional theory (DFT) calculations suggest that the enhanced selectivity of 2D Fe-SACs to produce NH_3 is attributed to a low energy barrier of 0.31 eV associated with the oxidation of *NO to *NHO. Then, we assembled the catalyst in a two- electrode electrolyzer connected to an InGaP/GaAs/Ge triple-junction solar cell and achieved a solar-to-ammonia (STA) conversion efficiency of 4.35% and a maximum yield rate of 0.29 mmol h^{-1} cm^{-2} equivalent to 5.10 mg h^{-1} cm^{-2}. These findings open new avenues for developing platinum group metal (PGM)-free single-atom catalysts (SACs) to realize the Haber-Bosch process using solar energy.

Electrochemical nitrate reduction reactions (eNO_3RRs) have been demonstrated to be an effective alternative approach in which nitrate is reduced to environmentally friendly nitrogen for water purification purposes.[1–3] Recently, nitrate-to-ammonia (NTA) conversion has been proposed and has stimulated tremendous interest *via* the eNO_3RR. Numerous catalysts have been developed to achieve NTA conversion, including monometals,[4–8] alloys,[9–12] transition metal oxides,[13–17] metal phosphides,[18] metal sulfides,[19] metal nitrides,[20] metal hydroxides,[21] metal oxyhydroxides,[22] metal-free catalysts,[23] and single/dual-atom catalysts.[24,25] Among these, single-atom catalysts (SACs), particularly Fe-based SACs, have garnered signifi- cant attention due to their earth abundance, low cost, high atomic utilization, and superior catalytic efficiency and selec- tivity in electrochemical nitrate reduction reactions (eNO_3RRs). Yu and co-workers[26] proposed a strategy based on a polymer hydrogel to create nitrogen-coordinated Fe sites with uniform atomic dispersion on carbon. The remarkable performance of Fe-based SACs is attributed to the single-site iron atoms occu- pying a nitrate-preoccupied transition center, effectively hindering water adsorption. Wang and colleagues[27] developed porous Fe single-atom catalysts (Fe-SACs) using a transition metal-assisted carbonization method. $FeCl_3$ and *o*-phenyl- enediamine precursors were used in the presence of SiO_2. These Fe-SACs exhibited impressive electrocatalytic properties for ammonia production. The research revealed that Fe single- atom catalysts effectively suppress the N–N coupling step required for the formation of N_2, thanks to the absence of neighboring metal sites.

However, most of the reported Fe-SACs for the eNO_3RR are three-dimensional (3D) bulk structures on a micrometer scale, with the Fe sites deeply embedded within the supports. This architecture leads to a low density of exposed active sites,

[a]*College of Bioresources and Materials Engineering, Shaanxi University of Science & Technology, Xi'an 710021, PR China. E-mail: liji@sust.eud.cn*

[b]*Institut Europeen des Membranes, IEM, UMR 5635, Universit´e Montpellier, ENSCM, CNRS, 34095 Montpellier Cedex 5, France. E-mail: damien.voiry@umontpellier.fr*

[c]*Departamento de Ciencia de los Materiales e Ingenier´ıa Metalu´rgicay Qu´ımica Inorga´nica, Facultad de Ciencias, Universidad de Ca´diz, Campus R´ıo San Pedro S/N, Puerto Real, 11510, Ca´diz, Spain*

[d]*Instituto Universitario de Investigaci´on de Microscop´ıa Electr´onicay Materiales (IMEYMAT), Facultad de Ciencias, Universidad de Ca´diz, Campus R´ıo San Pedro S/N, Puerto Real 11510, Ca´diz, Spain*

[e]*Chinese Academy of Sciences Dalian Institute of Chemical Physics, Dalian, 116023, PR China*

[f]*Southwest Jiaotong University, Research Institute of Frontier Science, Chengdu, Sichuan, 610031, PR China*

† Electronic supplementary information (ESI) available. See DOI: https://doi.org/10.1039/d4ta03824j

reduced mass/volume-specific activity, and sluggish mass transfer kinetics during the reaction.[28,29] In contrast, ultrathin two-dimensional (2D) Fe-SAC nanosheets offer several advan- tages. First, their large surface area facilitates close contact with the electrolyte and electrode, thereby enhancing charge transfer at the catalytic interface. Second, the highly open structure of the nanosheets exposes a greater number of interior atoms, resulting in highly accessible active sites for catalysis.[30] Take the zeolitic imidazolate framework (ZIF) derived Fe-SACs as an example, they exhibit a 3D rhomboid dodecahedron in shape. The nanosheet catalyst is a catalyst that has a 2D structure and a thickness that falls within the range of 1 to 20 nm. The ratio, denoted as R_s, between the accessible surface area of a two-dimensional material and that of a three-dimensional mate- rial, follows an inversely proportional relationship with the thickness of the two-dimensional material (see eqn (22)† and Fig. 2b). This clearly highlights that under identical synthetic conditions, two-dimensional single-atom catalysts exhibit greater potential in terms of high atomic utilization and cata- lytic activity for the eNO_3RR.

Additionally, for practical applications, the effective inte- gration of nitrate reduction catalytic systems with solar cells presents opportunities for wastewater valorization and sustainable green ammonia synthesis. However, solar-driven ammonia synthesis remains highly challenging, with the highest reported solar-to-ammonia (STA) efficiency for NH_3 production from N_2 still below 1%.[31–34] Moreover, there are very few studies on solar-driven ammonia synthesis using nitrate as the nitrogen source. Herein, we report a highly efficient inte- gration of GaInAs/Ga(In)As/Ge triple-junction solar cells with an electrochemical cell comprising 2D Fe-SACs for the NO_3RR and Pt for the oxygen evolution reaction (OER), achieving a STA efficiency of 4.35% for NH_3 production. Our 2D Fe-SACs exhibit exceptional activity and selectivity for the NO_3RR, with an onset potential of 0.1 V *vs.* RHE and a maximum faradaic efficiency of 95.4%.

To achieve the synthesis of a low-dimensional Fe single atom electrocatalyst, *i.e.* 2D Fe-SAC nanosheets, we have adopted a general salt-template confined *in situ* growth of Fe-doped ZIF-8 and pyrolysis strategy, see Scheme 1.[35] To begin with, nano- sheets of MOFs, which serve as precursors for 2D Fe-SAC nanosheets, were synthesized within the gaps of NaCl crystals. Subsequently, the nanosheets of MOFs and NaCl were pyrolyzed at a temperature of 900 °C under an Ar atmosphere. Following that, the Fe–NC nanosheets were purified with water and 5% dilute sulfuric acid solution three times, respectively. The morphology of as-synthesized 2D Fe-SACs was characterized by scanning electron microscopy (SEM) and transmission electron microscopy (TEM). As illustrated in Fig. 1a and ESI Fig. S1 and S2,† the 2D Fe-SACs have a crumpled sheet structure without any apparent presence of nanoparticles. Energy-dispersive X-ray spectroscopy (EDS) elemental mapping and electron energy loss spectroscopy in scanning transmission electron microscopy mode (STEM-EELS) were used to confirm the presence of Fe on carbon nanosheets. Insets of Fig. 1a, f and ESI Fig. S3, S5† show that the Fe, C, and N elements in the three products are distributed uniformly over the entire sample, with no metal NPs observed. This observation is supported by the absence of diffraction peaks from Fe metal or Fe oxides from our XRD analysis (ESI Fig. S6†). The thickness of our 2D Fe-SACs was measured by AFM (see Fig. 1b). The results show that their thickness is about 1.1 nm, inferred to be composed of approx- imately 2–3 layers of N-doped graphene loaded with Fe atoms.[36] To further investigate the morphology and structure of the catalyst, aberration-corrected high-angle annular dark-field scanning TEM (AC HAADF-STEM) analysis was performed. As shown in Fig. 1c, the brighter spots can be attributed to dispersed Fe atoms. For better observation, some Fe atoms were circled. All these results suggest that our catalyst exhibits two- dimensional and single-atom catalyst features (referred to as 2D Fe-SACs). We then performed Brunauer–Emmett–Teller (BET) analysis to determine the specific surface area of 2D Fe- SACs. Our results revealed a specific surface area of 77.4 m^2 g^{-1} which is higher compared to both the 3D Fe-SACs and the mesoporous Fe-SACs prepared using the same synthesis conditions (see ESI Fig. S7†). The Barrett–Joyner–Halenda (BJH) pore size distribution curves further revealed the presence of micropores measuring 1.9 nm in diameter, with a relatively small pore volume of 0.247 m^3 g^{-1}. These findings suggest that the catalytic reaction would primarily take place on the flat surface of the 2D Fe-SACs.

The chemical structure of the 2D Fe-SACs was further investigated using X-ray photoelectron spectroscopy (XPS). The high-resolution XPS spectra of the Fe2p region show two broad groups near 710.8 eV/710.8 eV along with a small but significant satellite near 720 eV that is likely associated with Fe^{2+} and Fe^{3+} (Fig. 1d).[37] The N1s spectrum is de-convoluted into four peaks at 398.02, 398.70, 399.34, and 401.04 eV which correspond to, respectively, pyridinic N, Fe–N, pyrrolic N, and graphitic N (see ESI Fig. S8†).[38] To investigate the electronic and coordination structure of 2D Fe-SACs, X-ray absorption near-edge spectros-copy (XANES) and extended X-ray absorption fine structure (EXAFS) analyses were performed. Fig. 1g shows the Fe K-edge XANES profiles for 2D Fe-SACs, Fe foil, Fe_2O_3, and FePc. The

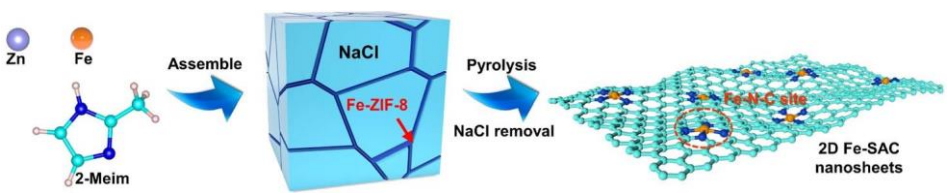

Scheme 1 Schematic illustration of the synthetic procedures for 2D Fe single-atom catalysts.

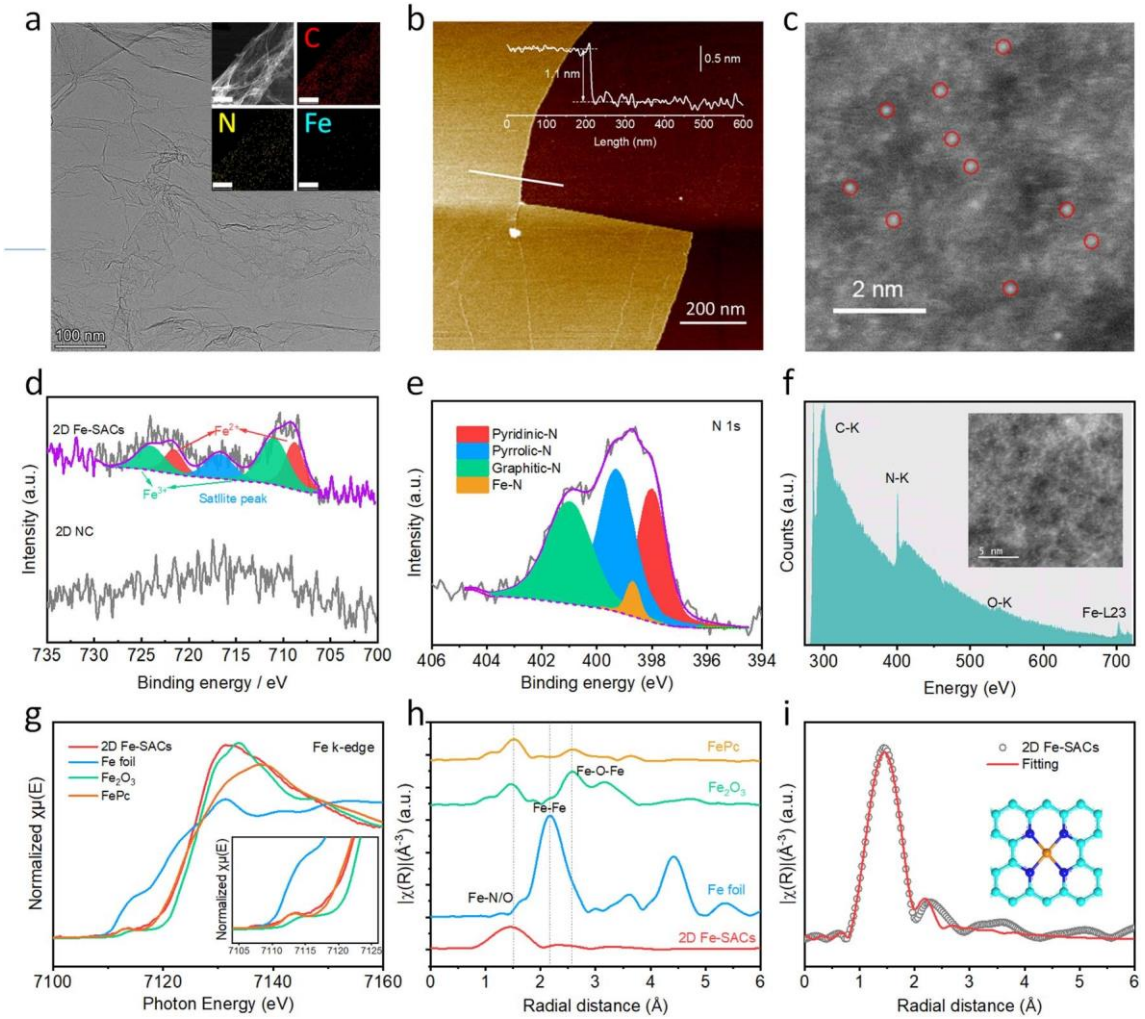

Fig. 1 (a) TEM images of 2D Fe-SAC nanosheets, scale bar = 100 nm, (inset: dark-field imaging transmission electron microscopy image of 2D Fe-SAC nanosheets and corresponding energy dispersive X-ray analyses (EDX), scale bar = 200 nm). (b) AFM images of the 2D Fe-SAC nano- sheets. (c) High-resolution HAADF-STEM image of 2D Fe-SAC nanosheets. (d) High-resolution XPS spectra of Fe 2p for 2D Fe-SAC nanosheets and 2D NC. (e) High-resolution XPS spectra of N 1 s for 2D Fe-SACs. (f) The EELS spectrum of 2D Fe-SACs. (g) Normalized XANES spectra at the Fe K-edge of the Fe foil, Fe_2O_3, Ferrous phthalocyanine (FePc), and 2D Fe-SACs. (h) The corresponding k3-weighted Fourier transform spectra. (i) Fitting results of Fe-MoS2 nanosheets, inset: its possible structure.

near-edge absorption energy position of 2D Fe-SACs was located between that of the FePc and Fe_2O_3, suggesting that the oxida- tion state of Fe in 2D Fe-SACs was between +2 and +3, which is in agreement with our XPS results.[39] The Fourier-transformed EXAFS curve of 2D Fe–SACs (see Fig. 1h) only shows one distinct peak at approximately ~1.5 Å, which was mainly attributed to the Fe–N/O first coordination shell. Moreover, no obvious Fe–Fe peak (2.2 Å) or other peaks are observed. To gain more information on structural parameters, least-square EXAFS fittings were performed (see Fig. 1i). The fitting parameters and results are summarized in ESI Table S1.† It shows that one Fe atom was coordinated by four N atoms at 1.96 Å forming a Fe– N4 moiety. Taken together, our findings point out the presence of individual iron atoms coordinated by nitrogen atoms sup- ported on ultra-thin nitrogen-doped carbon nanosheets as illustrated in the schematic presented in the inset of Fig. 1i.

Next, we evaluated the electrocatalytic performance of our catalysts for NO_3^- reduction by conducting electrochemical measurements in H-type cells with 0.1 M KOH and 0.1 M KNO_3 (the volume of both anode and cathode chambers was 30 mL). The LSV measurements were performed with and without NO_3^- at a scan rate of 20 mV s^{-1} and the polarization curve of 2D Fe- SACs was compared to those of three-dimensional Fe-SACs and mesoporous Fe-SACs (see Fig. 2a, the synthesis method is described in the experimental section of the ESI†). All the Fe single-atom catalysts with different structures displayed lower onset potentials and higher current densities in the presence of nitrate-containing electrolytes, indicating their effectiveness in selectively converting nitrate to ammonia. Among the catalysts tested, the 2D Fe-SACs exhibited the lowest onset potential of approximately 0.1 V *vs.* RHE compared to the 3D and meso- porous Fe single-atom catalysts. Conversely, no significant

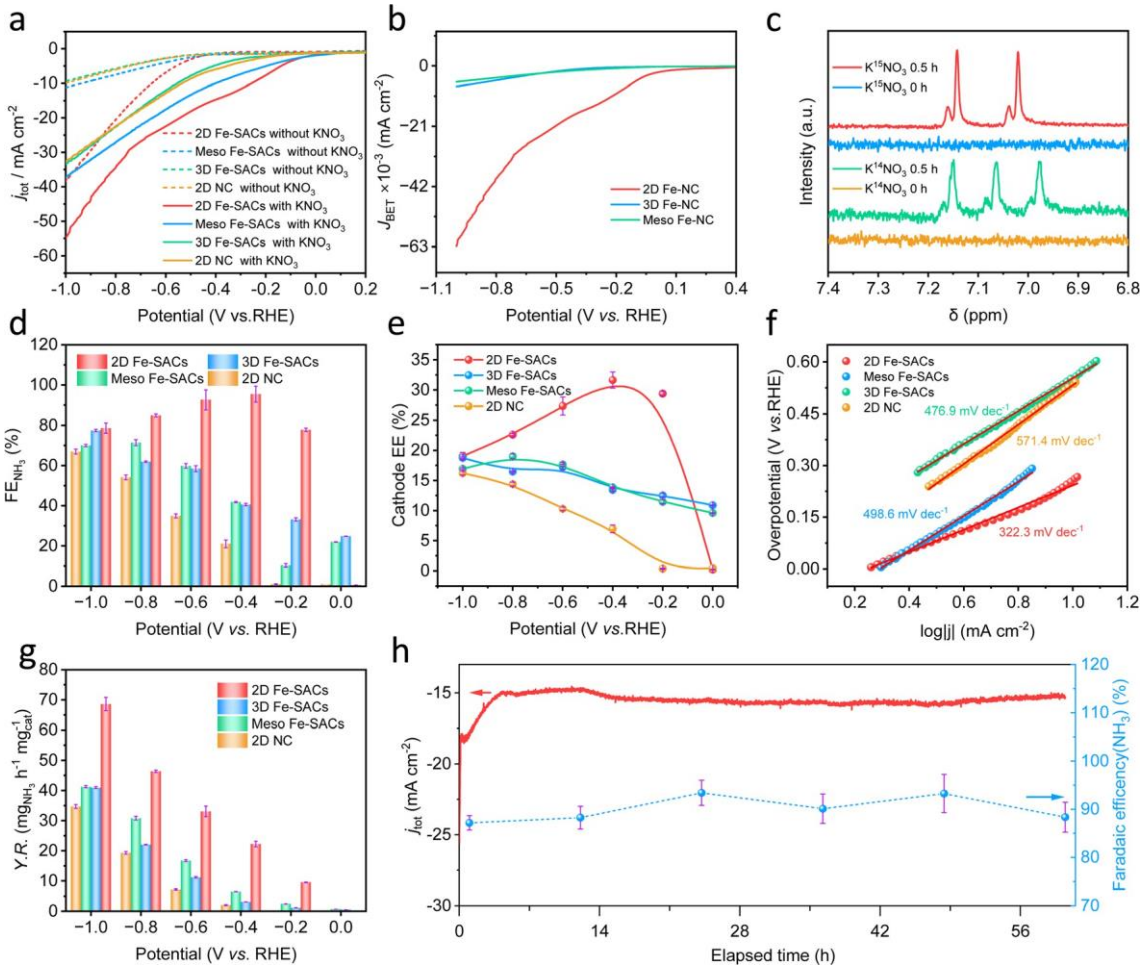

Fig. 2 The electrochemical performance investigation for the NO_3RR on 2D Fe-SACs. (a) LSV curves of 2D Fe-SAC, 3D Fe-SAC, Meso Fe-SAC, and 2D NC nanosheets with and without 0.1 M KNO_3 electrolyte. (b) BET normalized LSV curves of 2D Fe-SAC, 3D Fe-SACs, Meso Fe-SACs, and 2D NC nanosheets. (c) ^1H NMR spectra (600 MHz) of electrolyte produced from the NO_3RR under −0.40 V *versus* RHE on 2D Fe-SACs using 0.1 M $K^{14}NO_3$ and $K^{15}NO_3$ as electrolytes. (d) Potential-dependent faradaic efficiency of ammonia on 2D Fe-SAC, 3D Fe-SAC, Meso Fe-SAC, and 2D NC nanosheets. (e) The cathodic EE for NO_3^--to-NH_3 conversion on 2D Fe-SAC nanosheets compared with 3D Fe-SAC, Meso Fe-SAC, and 2D NC nanosheets. (f) Tafel slopes of the NO_3RR on 2D Fe-SAC, 3D Fe-SAC, Meso Fe-SAC, and 2D NC nanosheets. (g) Potential-dependent ammonia yield rate of the four types of catalysts in the presence of 0.1 M KNO_3 electrolyte. (h) NO_3RR stability at an applied potential of −0.40 V *vs.* RHE. Ammonia selectivity and current density are displayed for 60 h of operation.

differences were found in the geometric current densities of the three iron-based single-atom catalysts. Notably, despite having the smallest specific surface area among the three catalysts, as determined through specific surface area tests (see ESI Fig. S7 and Table S3 in the ESI†), the 2D Fe-SACs demonstrated clearly higher current densities when normalized to the BET-calculated specific surface area (Fig. 2b). This finding highlights the inherently superior catalytic activity of the 2D Fe-SACs in nitrate-to-ammonia conversion compared to the other two iron single-atom catalysts. The enhanced catalytic activity of the 2D Fe-SACs can be attributed to the abundant dispersion of isolated iron atoms on the surface of the synthesized 2D carbon nanosheets, facilitated by the templating synthesis method, as opposed to the iron atoms being embedded within the bulk carbon, which hinders mass transfer.

To exclude possible interferences and verify the reliability of UV-Vis detection in our experiments, isotopic experiments were carried out with 0.1 M $K^{14}NO_3$, 0.1 M $K^{15}NO_3$, and 0.1 M K_2SO_4, respectively. Fig. 2c shows the ^1H NMR spectra of the electrolytes after chronoamperometric experiments for 30 min, at −0.40 V *vs.* RHE. In the presence of $K^{15}NO_3$, two symmetric signals are detected at d = 7.02 and 7.14 ppm with a coupling constant of 73.1 Hz caused by the scalar interaction between ^1H and ^{15}N and can be assigned to $^{15}NH_4^+$. Conversely using $K^{14}NO_3$, three symmetric signals located at 6.99, 7.08, and 7.17 ppm with a coupling constant of 52.2 Hz in the electrolyzed electrolyte are observed and can be assigned to $^{14}NH_4^+$. These results suggest that ammonia is obtained by the electrochemical reduction of NO_3^- and does not result from external contamination. The concentration of NH_3 in the electrolyte was further quantified using ^1H NMR using an external standard and a previously reported colorimetric method (see ESI Fig. S13 and S14†).[40] The two analysis methods produced very similar results, indicating that

colorimetry offers satisfactory accuracy as a quantitative method for subsequent product measurements.

Fig. 2d and ESI Fig. S15† present the eNO$_3$RR performance of four kinds of catalysts at increasing overpotentials from 0 to −1.0 V *vs.* RHE. 2D Fe-SAC nanosheets displayed a volcanic shape curve with a maximum of 95.4 ± 4.0% at −0.40 V *vs.* RHE which is higher than that for 3D and mesoporous Fe SAC catalysts as well as 2D NC. This is due to the ultra-thin layered structure of 2D Fe-SACs, which means that most of the catalytic active sites are exposed on the surface, whereas, 3D Fe-SACs and Meso Fe-SACs possess active sites embedded within the pores despite their high specific surface area. Therefore, 2D Fe-SACs show higher faradaic efficiency for ammonia. To further quantify the catalytic properties of 2D Fe-SACs, we estimated the cathodic energy efficiency (EE_{NO_3RR}) of the Fe single-atom catalysts with different morphologies (Fig. 2e). The EE_{NO_3RR} for 2D Fe-SACs was found to be the highest at 31.6% for a cathodic potential of −0.40 V *vs.* RHE, which is at least 1.6 times higher than that of 3D Fe-SACs and Meso Fe-SACs. We then assessed the charge transfer resistance (R_{CT}) at the inter- face between 2D Fe-SACs and the electrolyte using electro- chemical impedance spectroscopy (EIS) (ESI Fig. S21†). By modeling the EIS responses with the Randles equivalent circuit, we determined the R_{CT} for the eNO$_3$RR on 2D Fe-SACs. The R_{CT} values are found to be relatively low in the case of 2D Fe-SACs at 31.4 U compared to 76.6 U for 3D Fe-SACs and 43.7 U for Meso Fe-SACs. These results point to faster kinetics for electron transfer at the surface of the catalyst in agreement with the reduction of the Tafel slope at 322 mV dec^{-1} compared to >450 mV dec^{-1} for 3D Fe-SACs and Meso Fe-SACs (Fig. 2f).

We further conducted a comparative analysis of the turnover frequency (TOF) for the three types of Fe single-atom catalysts in the context of their catalytic performance in ammonia produc- tion from nitrate (see ESI Fig. 16†). Notably, the 2D Fe-SACs demonstrated a superior turnover frequency across the entire range of tested applied potentials (ranging from 0 to −1.0 V *vs.* RHE). Collectively, these findings provide compelling evidence supporting the assertion that the notable intrinsic catalytic activity is attributed to the exposure of abundant loaded Fe single-atom active sites residing on the accessible surfaces of carbon nanosheets.

To better understand the behavior of 2D Fe-SACs, we explored the influence of Fe loading, pyrolysis temperature, nitrate concentration and pH value in the electrolyte. At −0.40 V *vs.* RHE, the faradaic efficiency continuously increases from 21.0% up to 95.4% as the Fe content is increased from 0% (*i.e.* 2D NC) to 0.83% (ESI Fig. S17†). The corresponding yield rate (YR) gradually increased and achieved a maximum of 22.2 ± 0.93 mg_{NH_3} h^{-1} mg_{cat}^{-1} for a loading of 0.47% of Fe on 2D carbon nanosheets. The effect of pyrolysis temperature on the catalytic performance is shown in ESI Fig. S18a and b.† The FE was maintained at a high level for the catalysts obtained at the five pyrolysis temperatures. We found however that the yield rate increased slowly with the increase of the pyrolysis temperature because increasing the pyrolysis temperature was beneficial to improve the conductivity of the catalyst. The effect of nitrate concentration on catalytic properties is shown in ESI Fig. S19a.† The greatest FE is 95% at 0.06 M electrolyte concentration and the FE showed a volcano trend as the electrolyte concentration decreased. We also observed that when increasing the nitrate concentration above that of the electrolyte, the primary by-product is nitrite. On the opposite, when the concentration of nitrate decreases, the evolution of hydrogen increases. The pH has a significant impact on the product selectivity of the NO$_3$RR using 2D Fe-SACs, with strong competition from the hydrogen evolution reaction at low pH levels. When the pH exceeds 3, the selectivity for NH_3 increases sharply to over 80%, while pH exerts minimal influence on the nitrite selectivity of the NO$_3$RR (see ESI Fig. S19b†). Thus, our two-dimensional single-atom iron-based catalyst demonstrates greater suitability for nitrate reduction under alkaline conditions in practical applications.

The ammonia YR of 2D Fe-SACs was found to reach a maximum of 68.6 ± 2.20 mg h^{-1} mg_{cat}^{-1} at −1.0 V *vs.* RHE, equivalent to 3.4 ± 0.11 mg h^{-1} cm^{-2}. This rate is at least 1.7 times higher than that of iron-based catalysts with 3D and mesoporous structures (Fig. 2g). Our 2D Fe-SACs exhibit superior performance compared to prior research on single-atom catalysts for the eNO$_3$RR (see ESI Table S2†). This enhancement in catalyst properties is ascribed to the two-dimensional structure of the Fe single atom's support and the improved kinetics at the active sites. To evaluate the stability toward the conversion of NO_3^--to-NH_3, we applied a steady-state potential on the 2D Fe-SAC electrode, while recording the current density and measuring the FE using colorimetry. Fig. 2h and ESI Fig. S20† show that the FE at −0.40 V *vs.* RHE displays minimal changes over 60 hours with an average value of 90.0 ± 2.8%. Although the current density shows a slight decline during the initial stages of the reaction, this phenomenon can be attributed to the generation and accumulation of a minor quantity of a gaseous byproduct (*i.e.* hydrogen). The robustness of the 2D Fe-SAC performance was further corroborated by the high retention of the current density and we demonstrated a 60 hour average yield rate of 22.1 ± 0.9 mg h^{-1} mg_{cat}^{-1} at −0.4 V *vs.* RHE.

To obtain more insight into the remarkable selectivity of the 2D Fe-SACs for the electrosynthesis of NH_3, we investigated the eNO$_3$RR on 2D carbon nanosheet SACs with various transition metals. Fig. 3a shows the polarization curves on 2D Fe-SACs, 2D Co-SACs, 2D Ni-SACs, and 2D Cu-SACs in the presence of NO_3^-. 2D Fe-SACs outperformed the other 2D carbon nanosheet SACs as evidenced by the larger current density and the lower onset potential compared to 2D Co-SACs, 2D Ni-SACs, and 2D Cu-SACs. The FE for NH_3 was found to vary between 37.5 and 44.1% at −0.4 V *vs.* RHE for 2D Co-SACs, 2D Ni-SACs, and 2D Cu-SACs , which is lower than that of 2D Fe-SACs at 95.4% (Fig. 3b). Remarkably the values of the onset potential for the NO$_3$RR, EE, and j_{NH_3} on 2D Fe-SACs are also respectively 2 to 14 fold higher, 2 times higher, and at least 200 mV lower (at j = 10 mA cm^{-2}) *vs.* RHE than the other 2D catalysts (Fig. 3a and c) – strongly suggesting that the dispersed Fe atoms on the 2D carbon nanosheets are key for enhancing the intrinsic catalytic activity and selectivity towards the NO$_3$RR.

To rationalize our experimental results, we conducted density functional theory calculations to investigate the NO$_3$RR

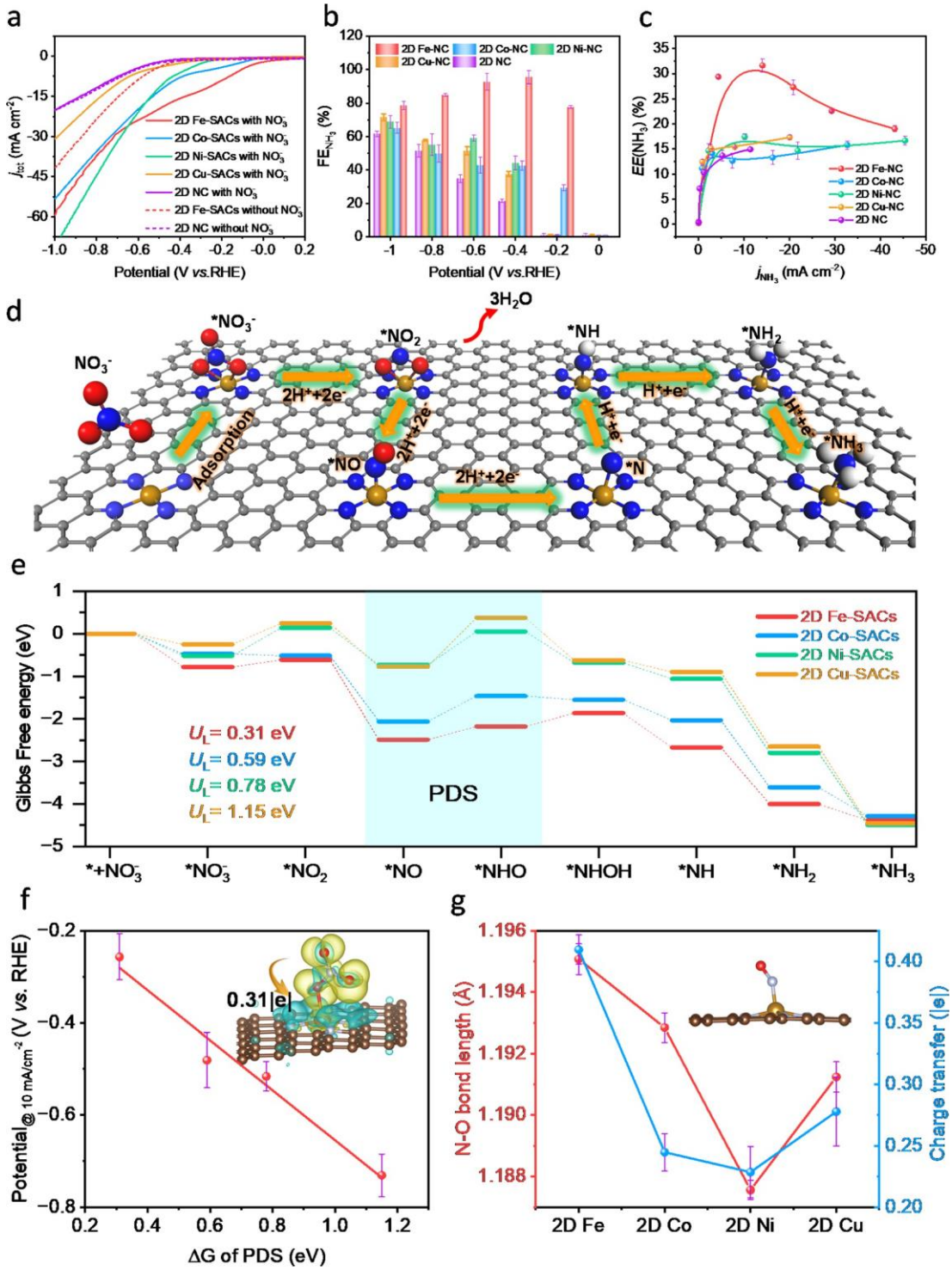

Fig. 3 The NO_3RR performance on 2D Fe-SACs compared with other 2D single-atom catalysts. (a) LSV curves of 2D Fe-SAC, 2D Co-SAC, 2D Ni- SAC, and 2D Cu-SAC nanosheets with and without 0.1 M KNO_3 electrolyte. (b) Potential-dependent faradaic efficiency of ammonia on 2D Fe-SACs nanosheets compared with 2D Co-SAC, 2D Ni-SAC, and 2D Cu-SAC nanosheets. (c) The cathodic EE for NO_3^--to-NH_3 conversion on 2D Fe-SACs compared with the other three 2D SAC nanosheets. (d) Reaction pathway for the NO_3RR on 2D M-SAC nanosheets (M: Fe, Co, Ni, and Cu, respectively). (e) Gibbs free energy diagram of the NO_3RR on 2D M-SAC nanosheets *via* the *NO／*NHO／*NHOH pathway. (f) The linear relationship between the Gibbs difference of the PDS and overpotential at j_{tot} = 10 mA cm^{-2} (inset: charge density difference plots for NO_3^- interaction with 2D Fe-SAC nanosheets). (g) Bader charge and N–O bond length analysis of the *NO intermediate on 2D M-SACs.

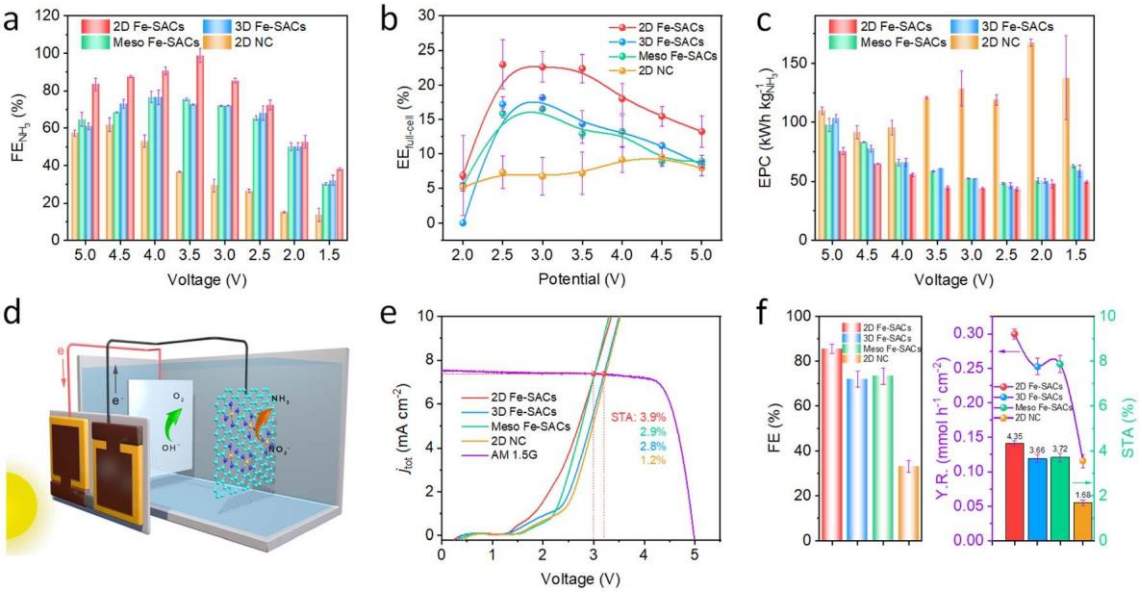

Fig. 4 The performance of 2D Fe-SACs for the NO_3RR using a 2-electrode electrolyzer. (a) Evolution of faradaic efficiency on 2D Fe-SAC, 3D Fe-SAC, Meso Fe-SAC, and 2D NC nanosheets as a function of the applied voltage. (b) The full cell EE for NO_3^--to-NH_3 conversion on 2D Fe-SAC nanosheets compared with 3D Fe-SAC, Meso Fe-SAC, and 2D NC nanosheets under different applied voltages. (c) Potential-dependent electric power consumption of ammonia of the full-cell device. (d) Schematic of the PV-electrolysis system for the conversion of nitrate to ammonia. (e) *J–V* characteristics of the triple junction solar cell under dark and simulated AM 1.5G 100 mW cm^{-2} illumination. Polarization curves of the full- cell device are based on four types of catalysts as NO_3RR catalysts at the cathode. (f) Faradaic efficiency, yield rate, and solar-to-ammonia conversion of four catalysts were evaluated for the NO_3RR in the PV-EC system under one-hour solar-driven catalysis.

on 2D carbon-based SACs with different transition metals including Fe, Co, Ni, and Cu atoms coordinated with 4 pyridinic nitrogens on graphene as presented in ESI Fig. S22.†[41] Fig. 3d and ESI Fig. S23† show the successive steps associated with nitrate reduction on the 2D carbon-based SACs, which can be decomposed into two main electrochemical processes: *NO_3^- / *NO_2 / *NO / *NHO (or *NOH) / *NHOH and *NH / *NH_2 / *NH_3 corresponding to deoxidation and hydrogenation mechanisms, respectively.[42,43] We first computed the Gibbs free energy of the full eNO_3RR pathway on the different 2D carbon-based SACs. All 2D carbon-based single-atom catalysts demonstrate comparable energy curves that bear resemblance to the eNO_3RR observed on Fe-MoS_2, as detailed in our prior study.[44] The potential-determining step (PDS) is associated with the *NO deoxygenation process (*i.e.* *NO / *NHO (or *NOH)). Compared with the *NO / *NOH pathway, the *NO / *NHO pathway exhibits a lower reaction energy barrier (see Fig. 3e and ESI Fig. S25†). Among the different metal single atoms, the lowest reaction free energy is obtained for 2D Fe-SACs at 0.31 eV. Concurrently, the Gibbs free energy change of the PDS exhibits a strong linear relationship with the overpotential value at a current density of 10 mA cm^{-2}, as derived from the LSV curve (see Fig. 3f). Consequently, the free energy change of the *NO / *NHO reaction can serve as a key indicator for screening novel 2D carbon-based SACs for the eNO_3RR in future research. To elucidate the origin of the reduced energy barrier for the PDS on the active sites, we examined the length bond of NO adsorption on each 2D carbon-based SAC, as shown in ESI Fig. S24† and 3g. We observed that the length of the NO bond is larger compared to the theoretical NO bond length of 1.15 Å, when adsorbed on the individual metal atom site.[45] The elongation of the NO bond is most pronounced on 2D Fe-SACs due to the activation effect of the Fe atom on *NO, which reduces the energy barrier for the eNO_3RR (ESI Table S4†). The d-band center of 2D Fe-SACs (1.22 eV and −0.363 eV) is closer to the frontier molecular orbital energy level of NO. Consequently, the Fe atom and NO are hybrided through electrons injected into the s* orbital of NO from the d-band of 2D Fe-SACs. Simultaneously, a feedback p bond is formed *via* donating electrons from the p* antibonding of NO to the d-band of 2D Fe-SACs near the Fermi level (see ESI Fig. S25†). Furthermore, it should be noted that with the increase in atomic number, the activation effect of the spin-polarized Fe, Co, and Ni atoms on *NO gradually diminishes. The trends of these activation effects are entirely consistent with the Bader charge analysis results between the various catalysts and *NO, as calculated (see Fig. 3g).

To evaluate the practical application potential of the three different morphologies of carbon-based Fe single-atom catalysts for ammonia production, we incorporated the catalysts into a 2-electrode H-cell reactor powered by an external photovoltaic (PV) cell. Initially, we evaluated the electrolytic properties of the full cell and systematically measured the FE as the cell voltage increased. The results indicate that under identical reaction conditions, the performance trends of the 2D Fe-SAC catalysts in the NO_3RR are similar in both two-electrode and three-electrode systems. However, the electrochemical window is wider, and the voltage is relatively higher in the two-electrode

system. This is because the two-electrode system lacks a reference electrode, making the working voltage the reaction potential difference between the working electrode and the counter electrode. Additionally, electrode surface polarization leads to a potential shi□, resulting in a higher voltage. Notably, the FE for NH_3 production by 2D Fe-SACs continuously increased up to 3.5 V, approaching a near-unity value (as shown in Fig. 4a). Fig. 4b and c provide an overview of the full cell energy efficiency (EE), the yield rate, and the electric power consumption (EPC, in kW h kg^{-1}) obtained by varying the voltage. The estimated $EE_{full\text{-}cell}$ is 24.2%, indicating the high energy-to-chemical conversion capability of our 2D Fe-SACs. Additionally, at a voltage of 3.5 V, the EPC was 46.6 kW h kg^{-1}, while the production rate reached 0.024 mmol h^{-1} cm^{-2}, corresponding to 412.6 mg h^{-1} cm^{-2}. We finally combined the 2-electrode H-cell reactor with photovoltaic cells to achieve indirect photo-catalytic conversion of nitrate to ammonia (Fig. 4d and ESI Fig. S25†). Given the higher potential required for electrochemical ammonia synthesis, achieving a reasonable efficiency in the experimental integration of photovoltaics and electrolysis processes is challenging. GaInAs/Ga(In)As/Ge triple-junction solar cells were utilized to generate adequate photovoltage to drive the catalytic reactions. Initially, the solar-to-ammonia conversion efficiency of the PV–EC system was predicted *via* analysis of the *I–V* characteristic curve of the solar cell and the polarization curves of the different catalysts for the eNO_3RR under dual electrodes. The solar-to-ammonia conversion efficiencies (STA) of 2D Fe-SACs, 3D Fe-SACs, and Meso Fe-SACs were estimated to be 3.9%, 2.9%, and 2.8%, respectively, as depicted in Fig. 4e. Notably, we found that the Fe-based SACs exhibit a 2 to 3-times increase in efficiency compared to STA without Fe single atoms, highlighting the promising potential of Fe-based SACs for effective eNO_3RR ammonia production. Our observations also indicate that two-dimensional single- atom catalysts surpass counterparts with different morphol- ogies in practical eNO_3RR ammonia production, attributable to the abundance of exposed active sites on their surfaces. Under AM 1.5G illumination for 1 hour, we determined that the production of ammonia reached 58.8, 49.5, 50.2, and 22.7 mmol of NH_3 on 2D Fe-SACs, 3D Fe-SACs, meso Fe-SACs and 2D NC, respectively. The rate of photocatalytic activity corresponds to approximately ~0.30 mmol h^{-1} cm^{-2} (see Fig. 4), which is equivalent to 5.10 mg h^{-1} cm^{-2}, surpassing previous reports on the photocatalytic NO_3RR (refer to ESI Table S3†). The estimated efficiency of solar-to-ammonia (STA) conversion is around 4.35%, which opens directions for feasible implementation of photocatalytic nitrate-to-ammonia conversion strategies.

Conclusion

Our report explored three distinct morphologies of carbon-based single-atom iron catalysts for the nitrate electro- chemical reduction to ammonia. Our investigations revealed that two-dimensional 2D Fe-SACs obtained through a salt- templating growth method exhibited superior electrocatalytic performance. At an overpotential of −0.40 V *vs.* RHE, 2D Fe-SACs achieved a remarkable FE of 95.4 ± 4.00% for NH_3. The high activity of 2D Fe-SACs towards the eNO_3RR can be attributed to both the strong interaction between the 2p* orbitals of *NO species and the d-band of iron atoms and the increased exposure of active sites at the interface accessible to the electrolyte owing to the two-dimensional nature of the carbon support. The high selectivity for ammonia combined with the improved kinetics on the nanosheet surface leads to a solar-to- ammonia (STA) conversion efficiency of approximately 4.35%, and a yield rate up to 0.29 mmol cm^{-2} h^{-1} powered by an external solar cell. Overall this study provides a guide for the design of the eNO_3RR for realizing autonomous ammonia production, opening directions for future applications in solar-driven NH_3 production.

Data availability

The data supporting this article have been included as part of the ESI.†

Author contributions

D. V. conceived the idea, designed the experiments and wrote the manuscript. J. L. designed the experiments with D. V., synthesized the materials, and performed the electrochemical measurements and the DFT calculations. J. L. and D. V. analyzed the data and wrote the manuscript. W. Z. and K. W. synthesized the materials and performed the physical charac- terization. E. P. carried out the NRM measurements. K. Q, Z. Y., and H. W. assisted J. L. with the electrochemical measurements.
J. L. performed the XAS on the samples with J.H. X. W. and Q. H. discussed the data with J. L. and D. V. L. L. performed high-resolution TEM and STEM of catalysts. T. Q fit the XANES with J. L. All of the authors edited the manuscript before submission.

Conflicts of interest

There are no conflicts of interest to declare.

Acknowledgements

D. V. acknowledges funding from the European Research Council (ERC) under the European Union's Horizon 2020 research and innovation programme (grant agreement No. 804320). D. V. acknowledges financial support from the US Army RDECom grant no. W911NF-17-2-0033. J. L. acknowledges financial support from the Youth Innovation Team of Shaanxi Universities (Education Department of Shaanxi Province, no. 22JP006) and Open Foundation of Key Laboratory of Auxiliary Chemistry and Technology for Chemical Industry, Ministry of Education, Shaanxi University of Science and Technology (no. KFKT2022-13) and Shaanxi Collaborative Innovation Center of Industrial Auxiliary Chemistry and Technology, Shaanxi University of Science and Technology (no. KFKT2022-13).

References

1 S. Han, H. Li, T. Li, F. Chen, R. Yang, Y. Yu and B. Zhang, *Nat. Catal.*, 2023, 6(5), 402–414.

2 H. Zhang, H. Wang, X. Cao, M. Chen, Y. Liu, Y. Zhou, M. Huang, L. Xia, Y. Wang, T. Li, D. Zheng, Y. Luo, S. Sun, X. Zhao and X. Sun, *Adv. Mater.*, 2024, 36, 2312746.

3 J. Liang, Z. Li, L. Zhang, X. He, Y. Luo, D. Zheng, Y. Wang, T. Li, H. Yan, B. Ying, S. Sun, Q. Liu, M. S. Hamdy, B. Tang and X. Sun, *Chem*, 2023, 9, 1768–1827.

4 M. Jiang, A. Tao, Y. Hu, L. Wang, K. Zhang, X. Song, W. Yan, Z. Tie and Z. Jin, *ACS Appl. Mater. Interfaces*, 2022, 14, 17470–17478.

5 M. Jiang, J. Su, X. Song, P. Zhang, M. Zhu, L. Qin, Z. Tie, J. L. Zuo and Z. Jin, *Nano Lett.*, 2022, 22, 2529–2537.

6 Y. J. Shih, Z. L. Wu, Y. H. Huang and C. P. Huang, *Chem. Eng. J.*, 2020, 383, 123157.

7 X. Deng, Y. Yang, L. Wang, X.-Z. Fu, J.-L. Luo, X. Deng, L. Wang, Z. X Fu, J.-L. Luo and Y. Yang, *Adv. Sci.*, 2021, 8, 2004523.

8 J. Chen, X. He, J. Li, X. Li, Z. Cai, Y. Luo, D. Zheng, T. Li, Y. Wang, Q. Liu, S. Sun, A. Farouk, M. S. Hamdy, X. Sun and B. Ying, *Inorg. Chem. Front.*, 2023, 10, 4450–4455.

9 J. X. Liu, D. Richards, N. Singh and B. R. Goldsmith, *ACS Catal.*, 2019, 9, 7052–7064.

10 F. Y. Chen, Z. Y. Wu, S. Gupta, D. J. Rivera, S. V. Lambeets, S. Pecaut, J. Y. T. Kim, P. Zhu, Y. Z. Finfrock, D. M. Meira, G. King, G. Gao, W. Xu, D. A. Cullen, H. Zhou, Y. Han, D. E. Perea, C. L. Muhich and H. Wang, *Nat. Nanotechnol.*, 2022, 17(7), 759–767.

11 Q. Gao, H. S. Pillai, Y. Huang, S. Liu, Q. Mu, X. Han, Z. Yan, H. Zhou, Q. He, H. Xin and H. Zhu, *Nat. Commun.*, 2022, 13(1), 1–12.

12 Y. Wang, A. Xu, Z. Wang, L. Huang, J. Li, F. Li, J. Wicks, M. Luo, D.-H. Nam, C.-S. Tan, Y. Ding, J. Wu, Y. Lum, C.-T. Dinh, D. Sinton, G. Zheng and E. H. Sargent, *J. Am. Chem. Soc.*, 2020, 142, 5702–5708.

13 R. Yang, H. Li, J. Long, H. Jing, X. Fu and J. Xiao, *ACS Sustain. Chem. Eng.*, 2022, 10, 14343–14350.

14 Y. Wang, W. Zhou, R. Jia, Y. Yu and B. Zhang, *Angew. Chem., Int. Ed.*, 2020, 59, 5350–5354.

15 R. Jia, Y. Wang, C. Wang, Y. Ling, Y. Yu and B. Zhang, *ACS Catal.*, 2020, 10, 3533–3540.

16 J. Wang, C. Cai, Y. Wang, X. Yang, D. Wu, Y. Zhu, M. Li, M. Gu and M. Shao, *ACS Catal.*, 2021, 11, 15135–15140.

17 X. Fan, C. Liu, Z. Li, Z. Cai, L. Ouyang, Z. Li, X. He, Y. Luo, D. Zheng, S. Sun, Y. Wang, B. Ying, Q. Liu, A. Farouk, M. S. Hamdy, F. Gong, X. Sun and Y. Zheng, *Small*, 2023, 19, 2303424.

18 Q. L. Hong, J. Zhou, Q. G. Zhai, Y. C. Jiang, M. C. Hu, X. Xiao, S. N. Li and Y. Chen, *Chem. Commun.*, 2021, 57, 11621–11624.

19 L. Yang and W. Zhu, *Appl. Surf. Sci.*, 2022, 596, 153624.

20 X. Zhang, G. Ma, L. Shui, G. Zhou and X. Wang, *Chem. Eng. J.*, 2022, 430, 132666.

21 W. Zheng, L. Zhu, Z. Yan, Z. Lin, Z. Lei, Y. Zhang, H. Xu, Z. Dang, C. Wei and C. Feng, *Environ. Sci. Technol.*, 2021, 55, 13231–13243.

22 F. Zhou, C. Sun, F. Zhou and C. Sun, *Small*, 2022, 18, 2200436.

23 L. Huang, L. Cheng, T. Ma, J. J. Zhang, H. Wu, J. Su, Y. Song, H. Zhu, Q. Liu, M. Zhu, Z. Zeng, Q. He, M. K. Tse, D. tao Yang, B. I. Yakobson, B. Z. Tang, Y. Ren and R. Ye, *Adv. Mater.*, 2023, 35, 2211856.

24 X. Zhao, X. Jia, Y. He, H. Zhang, X. Zhou, H. Zhang, S. Zhang, Y. Dong, X. Hu, A. V. Kuklin, G. V. Baryshnikov, H. Ågren and G. Hu, *Appl. Mater. Today*, 2021, 25, 101206.

25 Y. Zhang, Z. Yu, F. She, L. Wei, Z. Zeng and H. Li, *J. Colloid Interface Sci.*, 2023, 640, 983–989.

26 P. Li, Z. Jin, Z. Fang and G. Yu, *Energy Environ. Sci.*, 2021, 14, 3522–3531.

27 Z. Y. Wu, M. Karamad, X. Yong, Q. Huang, D. A. Cullen, P. Zhu, C. Xia, Q. Xiao, M. Shakouri, F. Y. Chen, J. Y. (Timothy) Kim, Y. Xia, K. Heck, Y. Hu, M. S. Wong, Q. Li, I. Gates, S. Siahrostami and H. Wang, *Nat. Commun.*, 2021, 12, 1–10.

28 L. Liu, T. Xiao, H. Fu, Z. Chen, X. Qu and S. Zheng, *Appl. Catal., B*, 2023, 323, 122181.

29 W. Da Zhang, H. Dong, L. Zhou, H. Xu, H. R. Wang, X. Yan, Y. Jiang, J. Zhang and Z. G. Gu, *Appl. Catal., B*, 2022, 317, 121750.

30 R. Yang, L. Mei, Z. Lin, Y. Fan, J. Lim, J. Guo, Y. Liu, H. S. Shin, D. Voiry, Q. Lu, J. Li and Z. Zeng, *Nat. Rev. Chem*, 2024, 8(6), 410–432.

31 C. Zhang, Y. Xu, C. Lv, X. Zhou, Y. Wang, W. Xing, Q. Meng, Y. Kong and G. Chen, *ACS Appl. Mater. Interfaces*, 2019, 11, 29917–29923.

32 Y. Bi, Y. Wang, X. Dong, N. Zheng, H. Ma and X. Zhang, *RSC Adv.*, 2018, 8, 21871–21878.

33 Y. Huang, Y. Zhu, S. Chen, X. Xie, Z. Wu and N. Zhang, *Adv.Sci.*, 2021, 8, 2003626.

34 W. Ren, Z. Mei, S. Zheng, S. Li, Y. Zhu, J. Zheng, Y. Lin, H. Chen, M. Gu and F. Pan, *Research*, 2020, 2020, 1–12.

35 L. Huang, X. Zhang, Y. Han, Q. Wang, Y. Fang and S. Dong, *J. Mater. Chem. A*, 2017, 5, 18610–18617.

36 C. Lee, X. Wei, J. W. Kysar and J. Hone, *Science*, 2008, 321, 385–388.

37 P. S. Bagus, C. J. Nelin, C. R. Brundle, B. V. Crist, N. Lahiri and K. M. Rosso, *J. Chem. Phys.*, 2021, 154(9), 094709.

38 T. Marshall-Roth, N. J. Libretto, A. T. Wrobel, K. J. Anderton, M. L. Pegis, N. D. Ricke, T. Van Voorhis, J. T. Miller and Y. Surendranath, *Nat. Commun.*, 2020, 11(1), 1–14.

39 L. Liu, T. Xiao, H. Fu, Z. Chen, X. Qu and S. Zheng, *Appl. Catal., B*, 2023, 323, 122181.

40 J. Li, Y. Zhang, C. Liu, L. Zheng, E. Petit, K. Qi, Y. Zhang, H. Wu, W. Wang, A. Tiberj, X. Wang, M. Chhowalla, L. Lajaunie, R. Yu and D. Voiry, *Adv. Funct. Mater.*, 2022, 32, 2108316.

41 T. Yang, T. T. Song, J. Zhou, S. Wang, D. Chi, L. Shen, M. Yang and Y. P. Feng, *Nano Energy*, 2020, 68, 104304.

42 D. Reyter, G. Chamoulaud, D. B´elanger and L. Rou´e, *J. Electroanal. Chem.*, 2006, 596, 13–24.

43 J.-X. Liu, D. Richards, N. Singh and B. R. Goldsmith, *ACS Catal.*, 2019, 9, 7052–7064.
44 J. Li, Y. Zhang, C. Liu, L. Zheng, E. Petit, K. Qi, Y. Zhang, H. Wu, W. Wang, A. Tiberj, X. Wang, M. Chhowalla, L. Lajaunie, R. Yu and D. Voiry, *Adv. Funct. Mater.*, 2022, 32, 2108316.
45 J. A. McCleverty, *Chem. Rev.*, 2004, 104, 403–418.